

Cluster and nebular properties of the central star-forming region of NGC 1140 ^{*}

S. L. Moll^{1†}, S. Mengel², R. de Grijs^{1,3}, L. J. Smith^{4,5} and P. A. Crowther¹

¹ *Department of Physics and Astronomy, University of Sheffield, Sheffield S3 7RH*

² *European Southern Observatory, D-85748 Garching, Germany*

³ *National Astronomical Observatories, Chinese Academy of Sciences, Beijing 100012, China*

⁴ *Space Telescope Science Institute and European Space Agency, Baltimore, MD 21218, U.S.A.*

⁵ *Department of Physics & Astronomy, University College London, London WC1E 6BT*

ABSTRACT

We present new high spatial resolution *HST*/ACS imaging of NGC 1140 and high spectral resolution VLT/UVES spectroscopy of its central star-forming region. The central region contains several clusters, the two brightest of which are clusters 1 and 6 from Hunter, O’Connell & Gallagher, located within star-forming knots A and B, respectively. Nebular analysis indicates that the knots have an LMC-like metallicity of $12 + \log \text{O}/\text{H} = 8.29 \pm 0.09$. According to continuum subtracted $\text{H}\alpha$ ACS imaging, cluster 1 dominates the nebular emission of the brighter knot A. Conversely, negligible nebular emission in knot B originates from cluster 6. Evolutionary synthesis modelling implies an age of 5 ± 1 Myr for cluster 1, from which a photometric mass of $(1.1 \pm 0.3) \times 10^6 M_{\odot}$ is obtained. For this age and photometric mass, the modelling predicts the presence of ~ 5900 late O stars within cluster 1. Wolf-Rayet features are observed in knot A, suggesting 550 late-type WN and 200 early-type WC stars. Therefore, $N(\text{WR})/N(\text{O}) \sim 0.1$, assuming that all the WR stars are located within cluster 1. The velocity dispersions of the clusters were measured from constituent red supergiants as $\sigma \sim 23 \pm 1 \text{ km s}^{-1}$ for cluster 1 and $\sigma \sim 26 \pm 1 \text{ km s}^{-1}$ for cluster 6. Combining σ with half-light radii of $8 \pm 2 \text{ pc}$ and $6.0 \pm 0.2 \text{ pc}$ measured from the F625W ACS image implies virial masses of $(10 \pm 3) \times 10^6 M_{\odot}$ and $(9.1 \pm 0.8) \times 10^6 M_{\odot}$ for clusters 1 and 6, respectively. The most likely reason for the difference between the dynamical and photometric masses of cluster 1 is that the velocity dispersion of knot A is not due solely to cluster 1, as assumed, but has an additional component associated with cluster 2.

Key words: galaxies: individual: NGC1140 – galaxies: starburst – galaxies: star clusters – stars: Wolf-Rayet

1 INTRODUCTION

Violent bursts of star formation, which are characteristic of starburst galaxies, resemble the star-forming phase of young galaxies in the early Universe. Nearby starbursts provide local templates to which distant star-forming galaxies may be directly compared. Only a handful of starburst galaxies are located within 10 Mpc, yet they produce around a quarter of the entire high-mass star population (Heckman

1998). Thus, starbursts are ideal sites in which to study massive stars. The signatures of Wolf-Rayet (WR) stars, which are the highly evolved descendants of massive O stars, are apparent in a subset of starburst galaxies, known as WR galaxies. Since WR stars are exclusively associated with young (~ 5 Myr) stellar populations, WR galaxies represent young or ongoing starbursts. A hallmark of all starbursts seems to be the production of luminous, compact star clusters. The sizes, luminosities and masses of these Young Massive Clusters (YMCs) are consistent with the properties expected of young globular clusters (GCs). This led to the suggestion that YMCs represent globular clusters at an early phase of their evolution. Dynamical mass measurements can potentially be used to test the scenario with respect to the long-term survivability of these YMCs (e.g. Ho & Filippenko 1996a,b; see de Grijs & Parmentier 2007

^{*} Based on observations collected at the European Southern Observatory, Chile, under programme ESO 71.B-0058(A), and on observations obtained with the NASA/ESA *Hubble Space Telescope*, which is operated by the Association of Universities for Research in Astronomy, Inc., under NASA contract NAS 5-26555.
[†] E-mail: s.moll@sheffield.ac.uk

for an overview). Understanding the role of YMCs as candidate proto-GCs is vital for our understanding of galaxy formation and evolution, as well as large-scale star formation. Clusters also have the advantage of being simple to model – they can be approximated as a coeval, simple stellar population with a single metallicity. This makes them ideal as probes of burst properties such as age, duration, chemical evolution and star-formation rate as well as constraining the parameters of the stellar initial mass function (IMF).

NGC 1140 is a low-metallicity WR galaxy at a distance of ~ 20 Mpc¹ and is a prime example of a nearby analogue of the star-forming galaxies identified at high redshifts. HI and optical observations indicate that the galaxy has undergone a merger within the past 1 Gyr and it is thought that this event is responsible for the plethora of YMCs that the galaxy hosts. Star clusters have been imaged with both the Wide Field/Planetary Camera (WF/PC) and the Wide Field Planetary Camera 2 (WFPC2) on the *Hubble Space Telescope* (*HST*) by Hunter, O’Connell & Gallagher (1994a) and de Grijs et al. (2004). They identified eight young luminous clusters in the centre of the galaxy, and their studies indicated that the clusters have masses of up to a few $\times 10^6 M_{\odot}$ and ages that lie in the range of a few to a few tens of Myr.

This paper considers the properties of the two brightest clusters within NGC 1140, clusters 1 and 6, and the two star-forming knots in which these clusters are contained. It is structured as follows. Details of our VLT and *HST* observations and data reduction are given in Section 2, along with photometry of the clusters. In Sections 3 and 4, we discuss the stellar and nebular properties of the two knots apparent in the VLT spectra, and in Section 5 we present the results of evolutionary synthesis modelling of cluster 1. The massive star population of cluster 1 and of both knots A and B, and the star-formation rate of NGC 1140, are considered in Section 6. The dynamical masses of the clusters are determined in Section 7 and we discuss our findings in Section 8. Finally, we summarise our results in Section 9.

2 OBSERVATIONS AND DATA REDUCTION

We obtained high-resolution spectroscopy of the central region of NGC 1140 with the VLT/Ultraviolet and Visual Echelle Spectrograph (UVES), in addition to high spatial resolution *Hubble Space Telescope* (*HST*) / Advanced Camera for Surveys (ACS) imaging of NGC 1140. Fig. 1 shows the region of the galaxy observed with UVES and labels clusters 1 – 7, as designated by Hunter et al. (1994a). It shows the location of the 1×11 arcsec² UVES slit, which was aligned north-south over the two knots in the central region of NGC 1140, hereafter called knots A and B. Knot A, which contains the clusters 1 and 2, is the brightest region in the optical and near infrared. Knot B lies ~ 3 arcsec south of knot A, and hosts clusters 5, 6 and 7.

¹ Based on the heliocentric velocity of the galaxy, corrected for the Virgocentric flow, and assuming $H_0 = 70 \text{ km s}^{-1} \text{ Mpc}^{-1}$; adopted from the *HyperLeda* database at <http://leda.univ-lyon1.fr/>

Table 1. F625W ACS aperture *STMAG* photometry of the brightest central clusters of NGC 1140 and the regions designated knots A and B. The F300W and F814W cluster magnitudes are taken from WFPC2 imaging of de Grijs et al. (2004).

Cluster	m_{F300W} (mag)	m_{F625W} (mag)	m_{F814W} (mag)
Cluster 1	16.50 ± 0.05	17.9 ± 0.1	18.51 ± 0.05
Cluster 2	16.37 ± 0.05	18.8 ± 0.1	19.11 ± 0.08
Cluster 6	18.47 ± 0.09	18.4 ± 0.1	18.73 ± 0.03
Cluster 7	21.71 ± 1.51	19.7 ± 0.1	19.86 ± 0.04
Knot A	15.5 ± 0.1	17.0 ± 0.1	17.8 ± 0.1
Knot B	17.6 ± 0.1	17.5 ± 0.1	18.4 ± 0.1

2.1 Imaging of NGC 1140

NGC 1140 was observed on 21 August 2003 with ACS/WFC aboard *HST* as part of GO programme 9892 (PI Jansen). Two exposures were taken – one of 950s duration with the narrow-band F658N filter and one of 100s duration using the broad-band F625W filter. The data were reduced using the on-the-fly reduction pipeline.

At the distance of NGC 1140, the F658N filter does not include the [N II] 6583 line, and, therefore, is essentially an H α plus continuum filter. We have corrected for the underlying continuum by subtracting the scaled F625W image such that a background galaxy is removed. This continuum subtracted F658N is included in Fig. 1. The high resolution of the ACS data also shows that clusters 3 and 5 from Hunter et al. (1994a) are not single clusters.

Aperture photometry was carried out on the drizzled F625W ACS image in Starlink’s GAIA. Since the crowded nature of the field makes it difficult to position apertures to include all of the light from the desired cluster without contamination from its neighbours, several circular apertures with a range of radii and positions were considered for each region. Each measurement was sky subtracted using a mean sky value obtained from several small apertures of sky, and aperture corrected using the values contained in Sirianni et al. (2005). As these aperture corrections are valid for point sources rather than for spatially extended clusters, our photometry may be an underestimate. However, since the light profile of the clusters is difficult to ascertain (see Section 7.1), no correction for this effect is made.

Table 1 presents our F625W photometry. The associated uncertainty represents the range of results produced. Table 1 also contains F300W and F814W photometry. The F300W and F814W photometry of knots A and B were determined using archival WFPC2 images (GO 8645, PI Windhorst) using the same method as described for the F625W images. The F300W and F814W cluster photometry was taken from de Grijs et al. (2004). The pre-COSTAR WF/PC photometry of de Grijs et al. (2004) and Hunter et al. (1994a) was not included due to its lower spatial resolution.

2.2 Spectroscopy of NGC 1140

The central region of NGC 1140 was observed with UVES on the VLT Kueyen Telescope (UT2) in Chile on 19-20 September 2003. UVES is a cross-dispersed echelle spec-

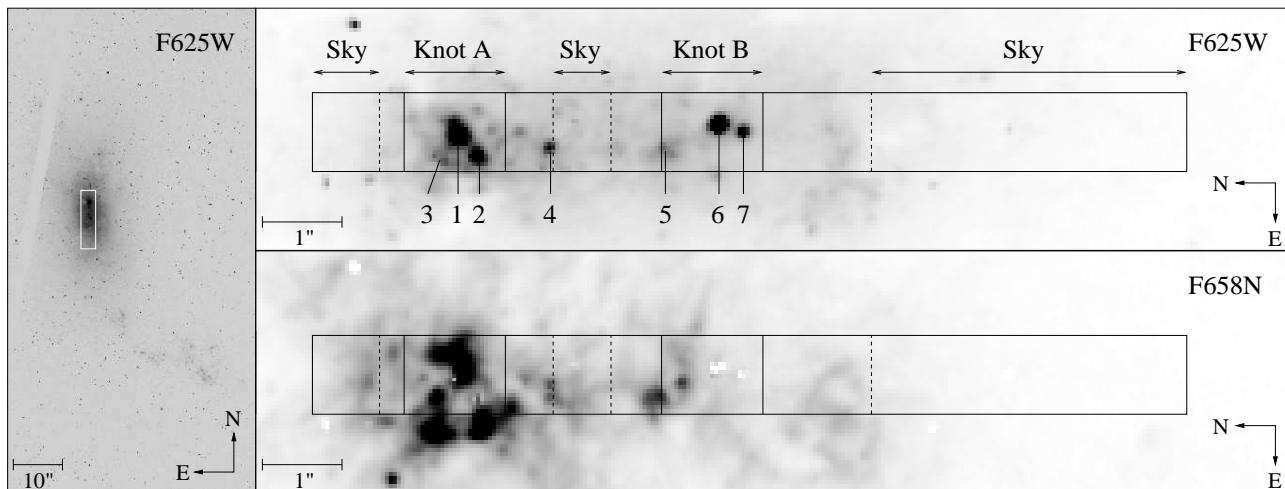


Figure 1. *HST*/ACS images of NGC 1140, at different cut levels (1 arcsec \sim 100 pc), marked as being either the F625W image or the continuum subtracted F658N image. The left-hand image shows the whole galaxy. The white box indicates the region that is magnified in the images in the right-hand panel. The lighter diagonal band across the image is the inter-CCD gap between the two detectors of ACS. Superimposed on each right-hand image is the 1×11 arcsec² VLT/UVES slit. The regions extracted as knots A and B and as sky are indicated by the solid and dashed lines, respectively. Clusters 1 – 7 (Hunter et al. 1994a) are also labelled. The top right-hand image shows that clusters 3 and 5 likely comprise several smaller clusters.

trograph, with two arms – a blue arm comprising a single EEV CCD and a red arm comprising a mosaic of an EEV and a MIT-LL CCD. Using the dichroic beam splitter, red and blue data were taken simultaneously: cross-disperser #4 with $312/\text{mm}^{-1}$ was centred on 840 nm and cross-disperser #2 with $660/\text{mm}^{-1}$ was centred on 437 nm. Thus, data from the regions $\sim 3740 - 4985\text{\AA}$ and $\sim 6475 - 10090\text{\AA}$ were obtained. The spectral region $\sim 8180 - 8420\text{\AA}$ was not observed since it lay on the gap between the two red CCDs. The data were 2×2 binned, so that the red data have a pixel scale of 0.364 arcsec pixel⁻¹ and the blue data have a scale of 0.512 arcsec pixel⁻¹.

The galaxy was observed with UVES for a total time of 14700s on the first night and 16200s on the second night. The seeing averaged ~ 0.8 arcsec on the first night, varying by ~ 0.1 arcsec and was somewhat poorer on the second night. The two knots were more clearly resolved in the data obtained on 19 September and so only the data of NGC 1140 from this night were considered in the analysis.

A telluric star, HIP 11918, was also observed in the same setup. Flux standards were not part of the original observing programme. However, we obtained data of two flux standards, EG274 and EG21. EG274 was observed for another programme on the first half of the first night for 600s using the blue setup above, plus a red setup centred on 8600\AA . EG21 was observed on the second night in 4 exposures of 2s in only the blue setup. ThAr arcs were taken for wavelength calibration. The resolution of the data, as measured from the ThAr arc lines, is $\sim 7 \text{ km s}^{-1}$.

The data were reduced using the software package IRAF. The data were bias corrected with a median bias frame, and divided by a normalised flat field. The two knots were extracted, each with an aperture of ~ 1.3 arcsec, and background subtracted using a polynomial fit to the sky regions indicated in Fig. 1. After extraction, median knot spectra were created and wavelength calibrated, before the orders were merged. The standard stars were similarly extracted.

This method over-subtracts the sky in the region of nebular lines. Therefore, the NGC 1140 spectra were also extracted without sky subtraction. The sky level was then manually subtracted with a polynomial fit so that the continuum matched that of the sky-subtracted spectra away from the nebular lines.

The blue NGC 1140 data were flux calibrated with EG274, and adjusted to match the F625W photometry of knot A and B contained in Table 1. Due to the lack of a suitable red flux standard, it was not possible to flux calibrate the red data. The calibrated blue spectrum of knot A is shown in Fig. 2, with the principal nebular lines indicated.

2.3 Spectroscopy of red supergiants

Comparison red supergiant (RSG) spectra are required to determine a cluster's velocity dispersion based upon its RSG features, which can then be used to calculate its dynamical mass. Therefore, six Small Magellanic Cloud (SMC) red supergiants, taken from the Massey & Olsen (2003) catalogue, were observed with the setup described above. The catalogue ID number of these stars, and their spectral types were 20133 (M0 I), 64448 (K2-7 I), 71566 (K7 I), 50840 (M1-2 I), 66694 (K5 I) and 71507 (K3-5 I).

3 STELLAR PROPERTIES

Red supergiant and OB stellar features are visible in the UVES spectra of both knots. Wolf-Rayet (WR) features are also present in the spectrum of knot A.

3.1 OB and WR star features

Knots A and B both show stellar absorption in the hydrogen Balmer series, arising from the presence of early-type stars, underlying strong nebular emission. The equivalent widths

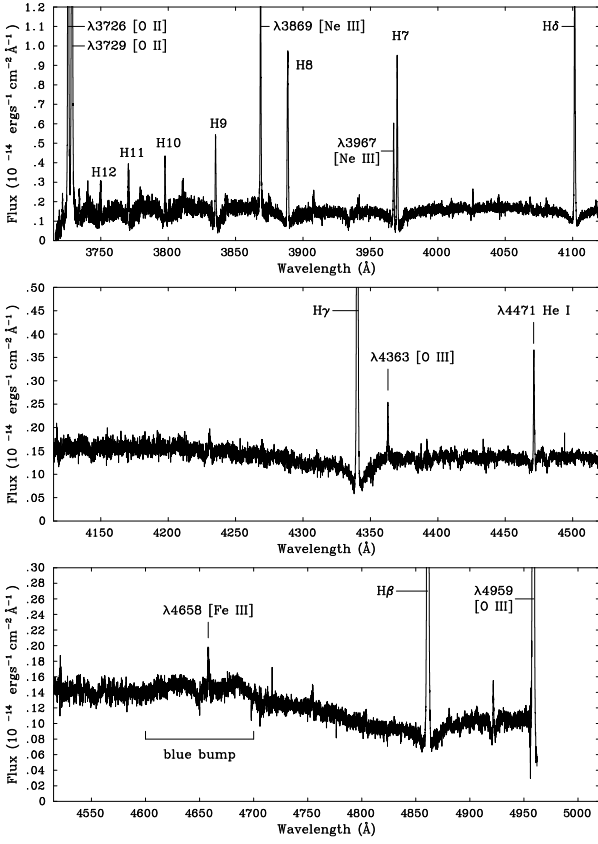


Figure 2. Blue spectrum of knot A with the principal nebular lines and the Wolf-Rayet blue bump marked, corrected to the stellar rest-frame. Broad stellar absorption is apparent underlying the narrow nebular Balmer emission.

of the underlying stellar absorption are $W_{\lambda}(\text{H}\beta) \sim 4\text{\AA}$, $W_{\lambda}(\text{H}\gamma) \sim 3\text{\AA}$ and $W_{\lambda}(\text{H}\delta) \sim 3\text{\AA}$.

WR stars are the bare cores of O stars, in their final evolutionary stages, characterised by strong, broad emission lines. Their strong winds reveal first the CNO-burning products, observable as nitrogen-rich (WN) stars and subsequently the He burning products, producing carbon-rich (WC) stars. A WR galaxy, or a cluster containing WR stars, can be identified by the presence of the blue bump around $\lambda 4686\text{\AA}$ or the yellow bump at $\lambda 5808\text{\AA}$ (Schaerer, Contini & Pindao 1999b). The yellow bump is produced solely by WC stars, while the blue bump can contain features of WN stars, such as stellar N III 4640 and He II 4686, and/or WC stars, such as C III 4650 and C IV 4658, with narrow nebular features superimposed, the strongest of which is [Fe III] 4658.

The blue WR bump emission feature in the spectrum of knot A has an equivalent width of $W_{\lambda} \sim 12.9\text{\AA}$, with He II 4686 contributing around $\sim 4.6\text{\AA}$. The presence of WR features in the spectrum of knot A constrains the age of the knot to 4 ± 1 Myr (Crowther 2007). No WR emission features are visible in the spectrum of knot B. The absence of WR stars implies that knot B is either younger than around 3 Myr, or older than around 5 Myr. However, the presence

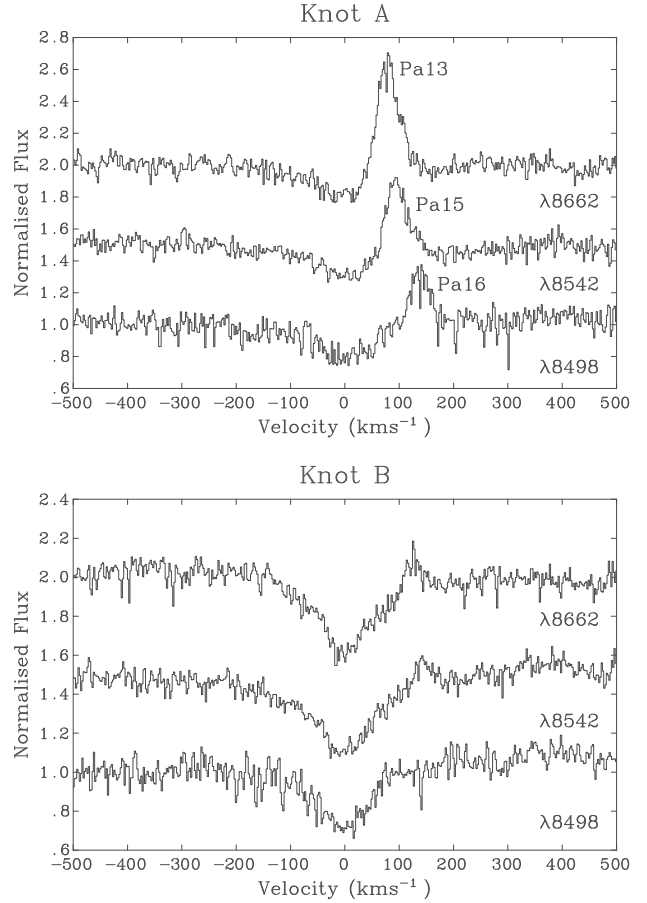


Figure 3. The normalised Ca II triplet lines of knot A (top) and knot B (bottom) after correction for a recession velocity of $v_r = 1475 \text{ km s}^{-1}$. The $\lambda 8542$ and the $\lambda 8662$ lines are offset by 0.5 and 1.0, respectively. Nebular Paschen emission lines are indicated.

of RSG features in the spectrum (see Section 3.2) makes it unlikely that the knot is younger than 3 Myr, for the case of an instantaneous burst.

3.2 RSG features

The Ca II triplet absorption lines ($\lambda\lambda 8498, 8542, 8662 \text{\AA}$) are clearly visible in the red spectra of both knots A and B. These features, along with other weak metal lines present in the data, such as Fe I and Mg I, arise from the RSGs in the cluster. The presence of RSGs indicates a cluster age greater than around 5 Myr.

The Ca II triplet lines of both knots were fitted with Gaussian profiles with the ELF (emission-line fitting) routine in Starlink's DIPSO package. The line centres, widths and intensity of the fits were allowed to vary freely, and the measured line centres used to determine the recession velocity of the galaxy. A good fit could not be obtained to the $\lambda 8542$ and $\lambda 8662$ lines of knot A, due to the presence of Paschen nebular lines within these profiles. Therefore, the recession velocities determined from the remaining four lines were averaged to obtain $v_r \sim 1475 \pm 4 \text{ km s}^{-1}$. Our result is

in good agreement with other recent values of recessional velocity, such as $v_r = 1498 \pm 33 \text{ km s}^{-1}$ from optical measurements (de Vaucouleurs et al. 1991), $v_r = 1501 \pm 1 \text{ km s}^{-1}$ from 21-cm HI observations (Haynes et al. 1998) and $v_r = 1480 \pm 9 \text{ km s}^{-1}$ from [Fe II] measurements (de Grijs et al. 2004).

After velocity correction, the equivalent widths of the Ca II triplet lines were measured with ELF, fixing the central wavelengths of the lines. This yields values of $W_\lambda(8498) = 0.77 \pm 0.07 \text{ \AA}$, $W_\lambda(8542) = 1.05 \pm 0.21 \text{ \AA}$ and $W_\lambda(8662) = 0.91 \pm 0.18 \text{ \AA}$ for knot A and $W_\lambda(8498) = 0.92 \pm 0.09 \text{ \AA}$, $W_\lambda(8542) = 2.2 \pm 0.3 \text{ \AA}$ and $W_\lambda(8662) = 1.45 \pm 0.15 \text{ \AA}$ for knot B. The velocity corrected Ca II triplet lines for knots A and B are presented in Fig. 3.

4 NEBULAR PROPERTIES

In this section we derive information on the gas dynamics of the knots from the profiles of the nebular lines. Extinctions, electron densities, temperatures and elemental abundances are determined from the relative fluxes of the nebular lines.

4.1 Line profiles and dynamics

Fig. 4 shows that the nebular H β profiles of knot A and knot B are very different. Knot A is dominated by one component at approximately $v \approx -15 \text{ km s}^{-1}$, but also has a weaker underlying broad component. Knot B more clearly comprises two components: a weaker component blueshifted at $v \approx -36 \text{ km s}^{-1}$ with FWHM $\sim 58 \text{ km s}^{-1}$ and a brighter redshifted component at $v \approx 28 \text{ km s}^{-1}$ with FWHM $\sim 47 \text{ km s}^{-1}$. These nebular profiles are representative of all the strong nebular lines of the knots. Examination of the 2D image indicates that there is diffuse emission throughout the central region of the galaxy that probably corresponds to the bluer, weaker component of knot B and to the weak, broad component of knot A. The stronger components of the knots arise from more discrete emission from the clusters within these knots, as are visible in Fig. 1. Alternatively, the broad underlying component of the knot A profiles may be due to hot cluster winds impacting on the surrounding interstellar clouds, as has been seen in other young star-forming regions (see Sidoli et al. 2006 for a review and Westmoquette et al. 2007 for a detailed discussion). Turbulent broadening of the order of 30 km s^{-1} was implied from the FWHMs of the main components of the strong nebular lines of knots A and B.

4.2 Line fluxes and extinction

Nebular line fluxes were measured by fitting the nebular emission with Gaussian profiles using the ELF routine, allowing line centres, widths and intensity to vary freely. The strong nebular emission of both knots A and B was fitted with two Gaussians (Section 4.1).

The internal extinctions of the knots, $E(B - V)_{\text{int}}$, were determined by comparing the observed flux ratios of $F(\text{H}\gamma)/F(\text{H}\beta)$ and $F(\text{H}\delta)/F(\text{H}\beta)$ to the intrinsic intensity ratios predicted by assuming Case B recombination theory for electron densities of 10^2 cm^{-3} and a temperature of 10^4 K (Hummer & Storey 1987). As the diffuse emission contained

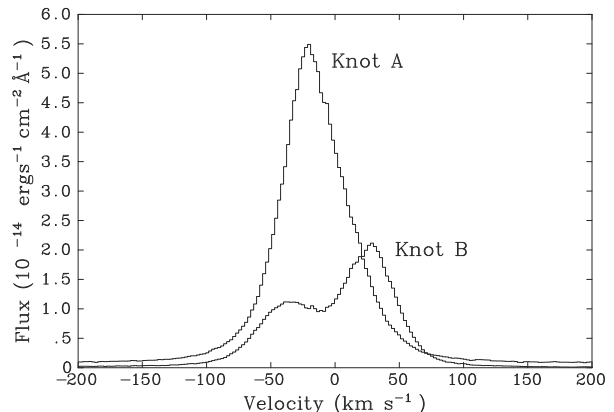


Figure 4. The H β profiles for knots A and B, after correction to $v_r = 1475 \text{ km s}^{-1}$.

Table 2. Comparison between predicted intrinsic flux ratios, $I_\lambda/I(\text{H}\beta)$ and observed flux ratios, $F_\lambda/F(\text{H}\beta)$. For the fluxes quoted here, both components of the knot A profile were summed, while only the strong redshifted component of knot B was considered. The observed ratios were first dereddened with a standard Galactic extinction law. Internal extinctions, $E(B - V)_{\text{int}}$, were then derived from predicted intensity ratios assuming a Howarth (1983) LMC extinction law.

	Line	$F_\lambda/F(\text{H}\beta)$ (Observed)	$I_\lambda/I(\text{H}\beta)$ (Predicted)	$E(B - V)_{\text{int}}$ (mag)
Knot A	H γ	0.427 ± 0.021	0.468	0.16 ± 0.10
	H δ	0.225 ± 0.011	0.259	0.16 ± 0.07
Knot B	H γ	0.427 ± 0.021	0.468	0.19 ± 0.10
	H δ	0.212 ± 0.011	0.259	0.27 ± 0.07

within knot B is expected to have a very low extinction compared to the discrete emission from the clusters, the nebular extinction was calculated based only on the stronger, redder component of knot B. Since the division between components is less well defined for knot A, both components were summed. The observed flux ratios were first corrected for foreground extinction of $E(B - V)_{\text{fore}} = 0.038 \text{ mag}$ (Schlegel, Finkbeiner & Davis 1998) using a standard Galactic extinction law before determining the internal extinctions of the knots using a Large Magellanic Cloud (LMC) extinction law (Howarth 1983). The ratios measured and internal extinction calculated are presented in Table 2. Ratios of H γ and H δ to H β were considered since H α was not flux calibrated. Mean values of $E(B - V)_{\text{int}} = 0.16 \pm 0.06 \text{ mag}$ for knot A and $E(B - V)_{\text{int}} = 0.23 \pm 0.08 \text{ mag}$ for knot B were subsequently adopted.

Table 3 presents observed and extinction corrected line fluxes, normalised to H $\beta = 100$. Here, both components were summed for both knots, as the total emission within the knot was of interest. Lines with total fluxes of $< 0.2\%$ of H β were not included. We concentrate on deriving the electron density, temperature and nebular abundances for knot A because of the added complications introduced by the nebular structure present in Knot B.

Table 3. Observed (F_λ) and intrinsic (I_λ) nebular line fluxes relative to $H\beta = 100$ for knot A and knot B. The fluxes quoted here are the summation of both components of the nebular lines, for both knots A and B. The intrinsic values are corrected for a foreground extinction of $E(B - V)_{\text{fore}} = 0.038$ mag with a standard Galactic extinction law and then for internal extinctions of $E(B - V)_{\text{int}} = 0.16 \pm 0.06$ mag for knot A and $E(B - V)_{\text{int}} = 0.23 \pm 0.08$ mag for knot B using the Howarth (1983) LMC extinction law. The flux of $H\beta$ is in units of $\times 10^{-14} \text{ erg s}^{-1} \text{ cm}^{-2}$.

Line	Knot A		Knot B	
	F_λ	I_λ	F_λ	I_λ
$\lambda 3726$ [O II]	65 \pm 3	82 \pm 7	81 \pm 4	112 \pm 12
$\lambda 3729$ [O II]	89 \pm 4	111 \pm 10	110 \pm 6	151 \pm 17
$\lambda 3869$ [Ne III]	21.0 \pm 1.0	25.5 \pm 2.0	20.0 \pm 1.0	26.1 \pm 2.5
$\lambda 3967$ [Ne III]	5.7 \pm 0.6	6.8 \pm 0.8	4.8 \pm 0.5	6.1 \pm 0.8
$\lambda 4026$ He I	0.89 \pm 0.18	1.05 \pm 0.22	0.89 \pm 0.18	1.11 \pm 0.23
$\lambda 4069$ [S II]	0.95 \pm 0.19	1.10 \pm 0.23	2.27 \pm 0.23	2.8 \pm 0.3
$\lambda 4102$ H δ	22.6 \pm 1.1	26.0 \pm 1.7	23.8 \pm 1.2	28.9 \pm 2.2
$\lambda 4341$ H γ	42.7 \pm 2.1	46.8 \pm 2.7	43.1 \pm 2.2	49 \pm 3
$\lambda 4363$ [O III]	1.5 \pm 0.15	1.63 \pm 0.17	1.03 \pm 0.10	1.16 \pm 0.12
$\lambda 4471$ He I	3.1 \pm 0.3	3.3 \pm 0.3	3.4 \pm 0.3	3.7 \pm 0.4
$\lambda 4658$ [Fe III]	1.08 \pm 0.11	1.12 \pm 0.11	2.22 \pm 0.22	2.33 \pm 0.23
$\lambda 4686$ He II	0.59 \pm 0.12	0.61 \pm 0.12	0.88 \pm 0.18	0.91 \pm 0.18
$\lambda 4702$ [Fe III]	0.52 \pm 0.10	0.53 \pm 0.11	—	—
$\lambda 4861$ H β	100	100	100	100
$\lambda 4959$ [O III]	98 \pm 5	96 \pm 5	96 \pm 5	94 \pm 5
H β	5.4 \pm 0.5	10 \pm 3	2.70 \pm 0.27	7 \pm 3

4.3 Electron densities and temperatures

The electron density, N_e , and electron temperature, T_e , of knot A were determined in the five-level atom calculator TEMDEN within IRAF using the diagnostic line ratios of [O II] $I(\lambda 3726)/I(\lambda 3729)$ and [O III] $I(\lambda 4363)/I(\lambda 4959)$. This gives values of $N_e = 60 \pm 50 \text{ cm}^{-3}$ (consistent with the low density limit) and $T_e = 9700 \pm 300 \text{ K}$.

4.4 Abundances

Knot A abundances were calculated from standard [O II] and [O III] diagnostics, plus the values of N_e and T_e determined in Section 4.3. These yield values of $N(\text{O}^+)/N(\text{H}^+) = (8.2 \pm 2.0) \times 10^{-5}$ and $N(\text{O}^{2+})/N(\text{H}^+) = (1.10 \pm 0.20) \times 10^{-4}$. These imply an abundance for knot A of $12 + \log \text{O}/\text{H} = 8.29 \pm 0.09$. We adopt this value for NGC 1140. It lies between the abundance of the Small Magellanic Cloud (SMC) of $12 + \log \text{O}/\text{H} = 8.13$ and that of the LMC of $12 + \log \text{O}/\text{H} = 8.37$ (Russell & Dopita 1990). It agrees well with other direct abundance measurements of NGC 1140 of 8.18 ± 0.06 (Izotov & Thuan 2004) and 8.26 ± 0.07 (Nagao, Maiolino & Marconi 2006; recalculated from the measurements of Izotov & Thuan 2004).

As the determined abundance is most similar to the LMC abundance, we adopt an LMC-like metallicity with $Z = 0.008$ for spectral modelling purposes.

Table 4. Equivalent widths and knot ages implied from the Starburst99 model. The equivalent width of Ca II is defined as $W_\lambda(\lambda 8542) + W_\lambda(\lambda 8662)$ (Díaz, Terlevich & Terlevich 1989).

Line	Knot A		Knot B	
	$W_\lambda(\text{\AA})$	Age (Myr)	$W_\lambda(\text{\AA})$	Age (Myr)
H α	289 \pm 29	5.5 \pm 0.5	142 \pm 14	6.0 \pm 0.5
H β	57 \pm 6	5.5 \pm 0.5	62 \pm 6	5.0 \pm 0.5
Ca II	1.96 \pm 0.28	5.5 \pm 0.5	3.7 \pm 0.3	≥ 6

5 PHOTOMETRICALLY DETERMINED CLUSTER PROPERTIES

Having established that knot A has an LMC-like metallicity and an age of around 5 Myr, we computed v5.1 Starburst99 evolutionary synthesis models (Leitherer et al. 1999; Vázquez & Leitherer 2005) for an instantaneous burst of star formation, with a total stellar mass of $10^6 M_\odot$ and a metallicity of $Z = 0.008$ for ages between 1 and 10 Myr in 0.5 Myr intervals. We adopted a Kroupa (2002) IMF (with slope $\alpha = 2.3$ for $0.5 \leq M/M_\odot \leq 100$ and $\alpha = 1.3$ for $0.1 \leq M/M_\odot < 0.5$) and Padova stellar evolutionary tracks (Fagotto et al. 1994), which include careful consideration of the RSG phase.

5.1 Age

The Starburst99 model predicts the equivalent widths for H α , H β and the Ca II triplet. The equivalent widths measured for each knot and the ages implied from the Starburst99 model are presented in Table 4.

Fig. 1 and Table 1 help to put these equivalent widths in context by showing the regions in which the continuum light and the nebular emission originate. In knot A, both the stellar continuum and nebular emission are dominated by cluster 1, indicating that the H α and H β equivalent widths are meaningful and can be applied to cluster 1. On the other hand, the stellar continuum of knot B is dominated by cluster 6, while the nebular emission is due solely to cluster 5 and a second source of emission ~ 0.4 arcsec immediately to the southwest of cluster 5. Therefore, these latter two sources must be younger than the 5 – 6 Myr quoted in Table 4. Indeed, the lack of Wolf-Rayet features in knot B indicates that they are younger than ~ 3 Myr. Fig. 1 shows no nebular emission from cluster 6 or 7, so these clusters must be older than ~ 10 Myr, unless any gas associated with these clusters has been removed by multiple supernovae at an even earlier stage. The equivalent widths of the Ca II triplet for both knots A and B are meaningful and can be applied to cluster 1 and 6, respectively, since these clusters dominate the continuum in the region. However, only a lower limit to the age of cluster 6 can be determined from the equivalent width of the Ca II triplet, because it does not vary strongly with age after a few Myr. Furthermore, the contribution of RSGs to cluster evolution is not well understood (e.g. Massey & Olsen 2003), and as such RSGs do not provide a reliable cluster age indicator.

After considering both the age indication of 4 ± 1 Myr from the presence of WR features in the spectrum of knot A and the realistic age estimates from Table 4, we adopt an

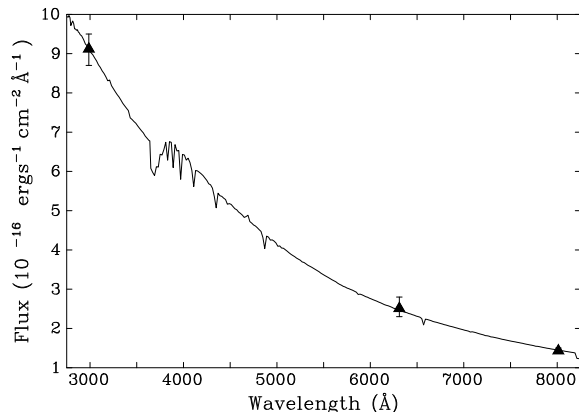


Figure 5. Fit of the reddened 5 Myr old model spectrum (Starburst99) to ACS and WFPC2 photometry for cluster 1. The model spectrum was first reddened by the foreground extinction of $E(B - V)_{\text{fore}} = 0.038$ mag (Schlegel et al. 1998) using a standard Galactic reddening law and then further reddened with a (Howarth 1983) LMC extinction law to best fit the plotted photometry.

age of 5 ± 1 Myr for knot A. Since no age can be estimated for cluster 6, it is not considered further in this section.

We find an age differential between knot A and knot B, in agreement with the results of both Hunter et al. (1994a) and de Grijs et al. (2004). Based on their $V - I$ colours, Hunter et al. (1994a) estimated the ages of the clusters in the region of knot A as ~ 3 Myr and interpreted the redder colours of the knot B clusters as being due to an older age of these clusters, as opposed to a higher extinction. They estimated the ages of these clusters as ~ 15 Myr, since this was the age determined by O’Connell, Gallagher III & Hunter (1994) for the YMCs in NGC 1569 and NGC 1705 with the same colours. The near infrared CIRPASS data of de Grijs et al. (2004) showed strong [Fe II] emission throughout the galaxy, while strong Br(12-4) and Br(14-4) was predominantly confined to knot A. Since the diffuse [Fe II] emission is likely associated with supernova remnants, while the Brackett nebular emission lines are associated with HII regions, de Grijs et al. (2004) argued that the ratio of these lines is a good age indicator. This would suggest that knot B is several Myr older than knot A.

5.2 Extinction

The model spectrum produced by the Starburst99 model for a 5 Myr old instantaneous burst was reddened to reproduce the ACS and WFPC2 photometry of cluster 1 (Table 1). The best fit, presented in Fig. 5, yields a value of internal cluster reddening of $E(B - V)_{\text{int}} \sim 0.24 \pm 0.04$ mag for cluster 1. The uncertainty quoted here solely considers the photometric uncertainties. The F300W and F625W photometry was more heavily weighted than the F814W photometry, since these are more sensitive to reddening. Our value agrees well with the result of de Grijs et al. (2004) of $E(B - V)_{\text{int}} = 0.14 - 0.26$ mag for cluster 2, determined from spectral energy distribution fits to their WF/PC and WFPC2 photometry. It also agrees with the nebular extinction determined from the Balmer lines, given in Table 2.

5.3 Photometric mass

The F625W magnitude for cluster 1 was converted into an apparent V -band magnitude using the transformation in Sirianni et al. (2005), assuming the Starburst99 model $V - R$ colour for a 5 Myr old burst and adopting the cluster extinction determined in Section 5.2. A distance of 20 Mpc to NGC 1140 then implies a V -band luminosity of $L_V = (7.3 \pm 1.8) \times 10^7 L_{\odot}$ for cluster 1. Comparing this luminosity to the Starburst99 prediction yields a photometric mass of $(1.1 \pm 0.3) \times 10^6 M_{\odot}$. This is based on a Kroupa IMF.

6 MASSIVE STAR POPULATION AND STAR-FORMATION RATE OF NGC 1140

In this section we determine the O star content of the knots from the $H\beta$ luminosity of the UVES spectroscopy. We estimate the WR content of knot A from the blue bump seen in its spectrum and measure the star formation rate (SFR) of NGC 1140 from the continuum subtracted F658N ACS imaging.

6.1 O star content

An estimate of the number of O stars within an individual knot can be obtained from the $H\beta$ luminosity, $L(H\beta)$. Assuming Case B recombination theory (Hummer & Storey 1987) and that a ‘normal’ stellar population is the only source of ionising photons within the knot, the number of equivalent O7V stars, $N(\text{O7V})$, contained within the knot is given by:

$$N(\text{O7V}) = \frac{Q_0^{\text{Obs}}}{Q_0^{\text{O7V}}} = \frac{L(H\beta) \times 2.1 \times 10^{12}}{Q_0^{\text{O7V}}}$$

(see e.g. Vacca 1994). Here, Q_0^{Obs} is the observed total Lyman continuum luminosity of the knot and Q_0^{O7V} is the Lyman continuum flux of an individual O7V star. distance of 20 Mpc and using the flux values given in Table 3, we obtain $L(H\beta) = (5.0 \pm 1.8) \times 10^{39} \text{ erg s}^{-1}$ for knot A and $L(H\beta) = (3.1 \pm 1.9) \times 10^{39} \text{ erg s}^{-1}$ for knot B. Taking $Q_0^{\text{O7V}} = 10^{48.9} \text{ photon s}^{-1}$, as suggested by Hadfield & Crowther (2006) for LMC metallicity O stars, implies that knot A contains 1300 ± 500 equivalent O7V stars and that knot B contains 800 ± 500 equivalent O7V stars. The Starburst99 modelling predicts an $H\beta$ luminosity for cluster 1 of $(4.5 \pm 1.1) \times 10^{39} \text{ erg s}^{-1}$, showing that cluster 1 dominates knot A in terms of its $H\beta$ luminosity. This implies the presence of 1200 ± 300 equivalent O7V stars within cluster 1.

This number of equivalent O7V stars can be converted into the total number of O stars, $N(\text{O})$, using the time-dependent parameter, $\eta(t)$:

$$N(\text{O}) = \frac{N(\text{O7V})}{\eta(t)}.$$

For an age of 5 Myr and a metallicity of $Z = 0.008$, Schaerer & Vacca (1998) give $\eta = 0.2$, implying that cluster 1 contains 5900 ± 1400 O stars. As knot A is dominated by cluster 1, applying $\eta = 0.2$ provides a good approximation to the number of O stars within knot A of 6600 ± 2400 .

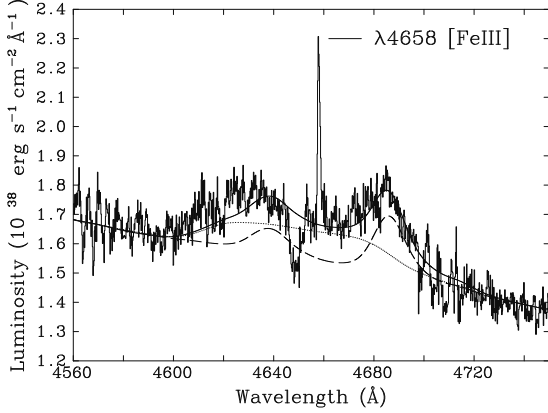


Figure 6. The $\lambda 4640$ Wolf-Rayet blue bump in the spectrum of knot A. The solid line shows the best empirical fit to the spectrum, of 550 WNL stars and 200 WCE stars. The dashed line shows only that from 550 WNL stars and the dotted line shows only the contribution from 200 WCE stars. Nebular [Fe III] $\lambda 4658$ emission is marked.

O stars. For knot B, which is dominated by the young cluster 5, the total number of O stars is comparable to the number of equivalent O7V, since $\eta \sim 1$ for ages of < 3 Myr (Schaerer & Vacca 1998).

6.2 Wolf-Rayet star content

The number of WR stars within knot A can be obtained by considering the luminosity of the blue WR bump. The similarity in the strengths of N III 4640 and He II 4686 in knot A suggests the presence of late-type WN (WNL) stars. The luminosity of $\lambda 4686$ is $6.8 \times 10^{38} \text{ erg s}^{-1}$, after correcting for an extinction of $E(B - V)_{\text{int}} = 0.24$ mag and a distance of 20 Mpc. Comparing this to the average luminosity of LMC WN7-9 stars of $(7.2 \pm 6.7) \times 10^{35} \text{ erg s}^{-1}$ (Crowther & Hadfield 2006), indicates that knot A contains 950 WNL stars, assuming no contribution to the blue bump from WC stars. However, Guseva, Isotov & Thuan (2000) identify early-type WC (WCE) stars in their long-slit spectrum of the entire central region of NGC 1140, by the presence of C IV 5808 emission. Therefore, we empirically match the blue bump using various multiples of an LMC WN7-9 star, plus an LMC WC4 star, finding a best fit of approximately 550 ± 100 WNL stars and 200 ± 50 WCE stars. This is shown in Fig. 6. We assume that all of the WR stars within knot A are contained in cluster 1, since it is the most massive young cluster within this region.

6.3 Star formation rate of NGC 1140

We measure an observed $\text{H}\alpha$ flux of $F(\text{H}\alpha) = (1.2 \pm 0.2) \times 10^{-12} \text{ erg s}^{-1} \text{ cm}^{-2}$ for the whole galaxy, based upon aperture photometry of the continuum subtracted F658N image (see Section 2.1). Assuming a distance of 20 Mpc and a mean extinction of $E(B - V)_{\text{int}} = 0.19$ mag, we find an $\text{H}\alpha$ luminosity of NGC 1140 of $(9 \pm 3) \times 10^{40} \text{ erg s}^{-1}$. This mean extinction was determined as an average of the nebular extinctions of knots A and B (Section 4.2) weighted by the

relative contributions to the $\text{H}\beta$ flux of the central region of 2:1 (taken from Table 3). Using the equation:

$$\begin{aligned} \text{SFR}(\text{M}_{\odot} \text{ yr}^{-1}) &= 7.9 \times 10^{-42} \times L(\text{H}\alpha) (\text{erg s}^{-1}) \\ &= 1.08 \times 10^{-53} \times Q_0^{\text{Obs}} (\text{photons s}^{-1}) \end{aligned}$$

(Kennicutt 1998), we estimate the SFR of the galaxy of $0.7 \pm 0.3 \text{ M}_{\odot} \text{ yr}^{-1}$, in good agreement with the SFR of $0.8 \text{ M}_{\odot} \text{ yr}^{-1}$, obtained from ground-based continuum subtracted $\text{H}\alpha$ imaging by Hunter, van Woerden & Gallagher (1994b), after adjustment to our adopted distance. Our $\text{H}\alpha$ luminosity gives $Q_0^{\text{Obs}} = (6.9 \pm 2.6) \times 10^{52} \text{ photons s}^{-1}$ or 9000 ± 3000 O7V equivalents in NGC 1140.

7 DYNAMICAL MASSES OF THE CLUSTERS

The virial motions of the individual stars within a cluster, as measured by the line-of-sight velocity dispersion, give a dynamical estimate of the cluster mass. This also requires a knowledge of the half-light radius of the cluster, which is the two-dimensional radius within which half of the projected luminosity of the cluster is contained.

7.1 Half-light radius

The half-light radii of clusters 1 and 6 were determined from the drizzled ACS/*HST* F625W images using the program ISHAPE (Larsen 1999). The routine convolves the point-spread function (PSF) of the camera with the desired light profile. ISHAPE computes a χ^2 minimisation between the cluster image and the model profile over a set fitting radius, iterating the FWHM, the ratio of the minor to major axes and the orientation of the fit. In order to obtain the best fit, the user specifies the ‘clean radius’, which is the largest radius that contains no contamination by neighbouring clusters.

Cluster 6 is more isolated than cluster 1, and is uncontaminated by its neighbours up to a clean radius of four pixels (1 pixel = 0.05 arcsec). Cluster 1, however, is only isolated up to two pixels. The half-light radii were computed by ISHAPE for a range of profiles, using a PSF that was computed in Tiny Tim (Krist & Hook 1997), for fitting radii between two and twenty pixels with a clean radius of two pixels for cluster 1 and four pixels for cluster 6. The profiles considered were a Gaussian profile, EFF profiles (Elson, Fall & Freeman 1987) of index x , which take the form:

$$f(z) = \frac{1}{(1 + z^2)^{\gamma}}, \quad \gamma = 0.1x$$

and King (1962) profiles of index c of the form:

$$f(z) = \begin{cases} \left(\frac{1}{\sqrt{1+z^2}} - \frac{1}{\sqrt{1+c^2}} \right)^2 & z < c \\ 0 & z \geq c. \end{cases}$$

There was a sudden jump in the values of half-light radii produced for fitting radii of eight pixels and for nine pixels. Therefore, the means of the half-light radii computed by ISHAPE for each profile for fitting radii between two and eight pixels were considered. These, along with the corresponding

Table 5. Mean half-light radii computed by ISHAPE for a range of model profiles for fitting radii between two and eight pixels, and the corresponding standard deviations (s.d.). Half-light radii were adopted on the basis of the best standard deviation.

Model	Index	Cluster 1		Cluster 6	
		r _{hl} (pc)	s.d.	r _{hl} (pc)	s.d.
Gaussian	—	6.1	0.8	5.6	0.4
EFF	15	9.5	0.5	8.4	0.5
EFF	25	6.9	0.8	6.12	0.12
King	5	6.6	0.8	5.79	0.12
King	15	8.2	0.5	7.0	0.6
King	30	10.4	0.4	8.8	1.2
King	100	17.3	0.6	14.6	2.6
Adopted		8 ± 2		6.0 ± 0.2	

standard deviation, are contained in Table 5. As a good profile fit will not vary much with fitting radius, the profile with the lowest standard deviation was adopted. For cluster 1 this was the King 30 profile. However, the standard deviation of this is quite large and similar to that produced for other profiles. Discarding the outlying values produced by the King 100 profile, the mean and standard deviation of the 42 results produced by the other 6 profiles gives $r_{hl} = 8 \pm 2$ pc for cluster 1.

For cluster 6, both the EFF 25 and the King 5 profile show an equally high level of consistency and a mean of the results of both of these profiles was adopted to give $r_{hl} = 6.0 \pm 0.2$ pc for cluster 6.

7.2 Velocity dispersion

The line-of-sight velocity dispersion, σ , of a cluster can be determined by comparing the broadening in the lines of the cluster spectrum with respect to those in a red supergiant template spectrum. There are two main methods that quantify the comparison, and these are discussed below.

The spectrum is compared to red supergiant templates because the lines of these stars are broadened by only a few km s^{-1} , by macro-turbulence in their atmospheres (Gray & Toner 1986). It is not appropriate to use earlier type supergiants and main sequence stars, as effects such as rotational broadening, macro-turbulence and micro-turbulence broaden the lines of these stars by amounts comparable to the anticipated cluster velocity dispersions. Therefore, only spectral regions redwards of $\sim 5000\text{\AA}$, which are dominated by light arising from cool supergiants of spectral type F-M, should be considered (see e.g. Ho & Filippenko 1996a). Suitable spectral regions should show visible similarity between the cluster and RSG spectra and should also not contain any telluric lines, which provide an artificial match between the spectra.

The first method relies on minimising a reduced χ^2 between the normalised cluster spectrum and normalised, broadened template spectra. The broadening is achieved by convolving the normalised template spectrum with a Gaussian of σ equal to the desired velocity broadening. The broadened template is multiplied by an optimum factor, so that it produces the lowest possible reduced- χ^2 between the broadened template spectrum and the cluster spectrum. The

Table 6. Values of line-of sight velocity dispersion over the region 8485 – 8845Å for each red supergiant template observed. The templates are identified by their Massey & Olsen (2003) catalogue number. It is marked whether the cross-correlation (Xcor) or χ^2 minimisation (χ^2) technique was used. The Paschen emission was masked out for the reduced χ^2 minimisation technique. The results obtained for the cross-correlation technique are an upper limit on the cluster velocity dispersion.

RSG Template Cat No.	Spectral Type	Velocity dispersion (km s^{-1})		
		Cluster1 χ^2	cluster 6 Xcor	cluster 6 χ^2
64448	K2-7 I	23	26	26
30840	K3-5 I	23	29	27
66694	K5 I	23	30	26
71566	K7 I	22	29	26
20133	M0 I	24	31	27
50840	M1-2 I	22	32	26
Mean		24	30	26

template is broadened by a range of suitable values and a reduced- χ^2 is similarly computed for each value of broadening. The lowest of these χ^2 values determines what amount of broadening produces the best match with the cluster for a given template, and so indicates the velocity dispersion of the cluster. This is repeated for a range of template spectral types. This method relies on a good match between the relative line strengths of the cluster and template and can thus be sensitive to the spectral type of the template star.

The second method utilises the cross-correlation technique of Tonry & Davis (1979). It requires that the spectra being considered are normalised, and continuum subtracted, to give a flat continuum at zero. The cluster is then cross-correlated with a red supergiant template over suitable spectral regions, and the FWHM of the resulting cross correlation function (CCF) is measured. The template spectrum is broadened by a range of velocities. Each broadened template is cross-correlated with the original, unbroadened template and the FWHM of each CCF is measured. In this manner, the near-linear relationship between broadening and the FWHM of the CCF can be empirically calibrated to an absolute scale. This calibration is applied to the FWHM of the original CCF, produced by cross-correlating the cluster spectrum with the template spectrum, to determine the velocity dispersion of the cluster. This is repeated for each template star. The conversion factor differs with template spectrum. While this method is less sensitive to spectral type matching, it suffers from complications associated with the subjectivity of fitting CCFs. These include factors such as selecting the background level and fitting non-Gaussian CCFs, and are especially important when the CCF is weak.

Since clusters 1 and 6 are the brightest cluster members in knots A and B, we assume that the velocity dispersions of these clusters dominate the broadening of the RSG features apparent in the knots.

Unfortunately, the youth of cluster 1 means that the RSG features in the spectrum are very weak, and many of the lines visible in the template spectra are absent in the cluster spectrum. The low signal-to-noise ratio of knot B causes a similar problem. The strongest RSG features, the

Ca II triplet absorption lines, are clearly visible in the cluster spectra. However, these lines are saturated in the template spectra. As the core of a saturated profile is narrower than would have been produced in a Gaussian profile, and it is the core that produces the CCF signal, cross-correlation of these regions tends to overestimate the cluster velocity dispersion (see e.g. Walcher et al. 2005). However, cross-correlation of all other regions that both contain RSG features and lack telluric features produce very noisy, non-Gaussian CCFs, which cannot be robustly fitted. Therefore, only the region 8485 – 8845 Å was considered for cross-correlation. Cross-correlation of even this region of knot A with the templates did not produce CCFs that could be confidently fitted, likely due to the contamination of the Ca II triplet by the strong Paschen lines. Therefore, no results were produced for knot A using the cross-correlation technique.

The reduced- χ^2 minimisation could also only be computed for the region 8485 – 8845 Å, due to the lack of strong RSG absorption lines except around the Ca II triplet. The Paschen emission features were masked out of both knot spectra before the reduced- χ^2 minimisation was computed. The results of the cross-correlation and the reduced- χ^2 minimisation are listed in Table 6.

The results show consistency over all the spectral types, with the cross-correlation of cluster 6 with the templates producing systematically higher velocity dispersions than the reduced- χ^2 technique, as expected. There should not be any systematic uncertainties in the velocity dispersion calculated by reduced- χ^2 minimisation, despite the use of the Ca II triplet lines. Mengel et al. (2002) found no disparity between the velocity dispersion results computed by χ^2 minimisation for the strongest component of the Ca II triplet and other individual absorption features for clusters in NGC 4038/4039. The mean and standard deviation of the velocity dispersions calculated from the reduced- χ^2 minimisation from all six template stars give values of $\sigma = 24 \pm 1 \text{ km s}^{-1}$ for cluster 1 and $\sigma = 26 \pm 1 \text{ km s}^{-1}$ for cluster 6.

7.3 Virial mass

The virial equation relates the virial mass of a cluster, M_{dyn} , to the line-of-sight velocity dispersion, σ , and the half-light radius, r_{hl} , of the cluster by the equation:

$$M_{\text{dyn}} \approx \frac{\eta \sigma^2 r_{\text{hl}}}{G}.$$

This equation assumes that a cluster is gravitationally bound, spherically symmetrical and virialised, that the velocity dispersion of the cluster is isotropic and that all of the stars contained in the cluster are single stars of equal mass. Spitzer (1987) showed that $\eta = 9.75$ for globular clusters with a wide range of light profiles. However, mass segregation and the presence of binary stars within the cluster can cause a large variation in the value of η (Boily et al. 2005; Fleck et al. 2006; Kouwenhoven & de Grijs, in prep.). For the young age and high mass of cluster 1, however, these effects are minimal. Table 7 summarises the cluster properties.

Table 7. Summary of cluster properties of clusters 1 and 6.

Property	cluster 1	cluster 6
$E(B - V)(\text{cluster})$ (mag)	0.24 ± 0.04	—
Age (Myr)	5 ± 1	—
r_{hl} (pc)	8 ± 2	6.0 ± 0.2
σ (km s^{-1})	24 ± 1	26 ± 1
$M_{\text{dyn}} (10^6 M_{\odot})$	10 ± 3	9.1 ± 0.8
$L_V (10^7 L_{\odot})$	7.3 ± 1.8	—
$L_V / M_{\text{dyn}} ((L_V / M)_{\odot})$	7.0 ± 2.6	—

8 DISCUSSION

In this section we discuss the disparity found between the dynamical and photometric mass estimates. We also consider the reliability of stellar evolution models by comparing them with observations.

8.1 How reliable are photometric mass estimates versus dynamical mass estimates?

The dynamical mass determined for cluster 1 is several times greater than the photometric mass found. To assess this disparity, Fig. 7 compares the light-to-dynamical mass ratio of the cluster to a model light-to-mass ratio at the known age of the cluster. The model assumes Maraston (2005) SSPs, a Kroupa IMF and solar metallicity. Data for several other clusters whose velocity dispersions were measured from UVES observations are also included. It is clear from this figure that many other young (< 20 Myr) clusters also have light-to-dynamical mass ratios well below model predictions, while the older (> 20 Myr) clusters have ratios that agree well with the canonical value.

As discussed by Bastian et al. (2006) and Goodwin & Bastian (2006), the most likely explanation for the discrepancy between model and observations seen in the sample of young clusters is a lack of virial equilibrium caused by violent relaxation after the formation of the cluster and from the expulsion of gas. This causes the measured dynamical mass to overestimate the true mass. Since the older clusters, which are expected to be in virial equilibrium after surviving gas expulsion, lie on or near the model line, the photometric mass is likely to be a good representation of the true cluster mass. This supports the assumption of a standard IMF. In this case, the disagreement between the dynamical mass and the photometric mass of a cluster can be used to assess to what degree the cluster is out of virial equilibrium. This can be parameterised by the effective star formation efficiency (eSFE) of the cluster, ϵ ; at the onset of gas expulsion, a cluster with an eSFE = ϵ has a velocity dispersion that is $\sqrt{1/\epsilon}$ too large to be in virial equilibrium (Goodwin & Bastian 2006). The model light-to-mass ratio assuming a range of effective star formation efficiencies are included in Fig. 7, taking the onset of gas expulsion as 2 Myr. These tracks differ from those presented by Goodwin & Bastian (2006) as they are not smoothed.

An alternative explanation for clusters lying below the canonical line in Fig. 7 is that these clusters have non-standard IMFs. In this situation, the dynamical mass represents the true cluster mass, and the incorrect assumption of a

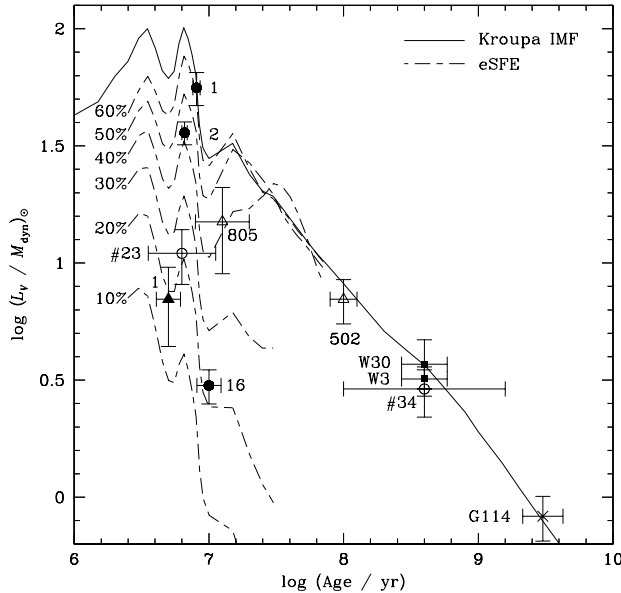


Figure 7. Diagram of light to dynamical mass ratio against age for cluster 1 in NGC 1140 (filled triangle; this work), and for clusters 1, 2 and 16 in NGC 4038/4039 (filled circles; Mengel et al. 2002), clusters 502 and 805 in NGC 5236 (open triangles; Larsen & Richtler 2004), clusters W3 (Maraston et al. 2004) and W30 (Bastian et al. 2006) in NGC 7252 (filled squares), cluster G114 in NGC 1316 (cross; Bastian et al. 2006) and clusters #23 and #34 in ESO 338-IG04 (open circles; Östlin et al. 2006). Also plotted are the model evolution of light-to-mass ratio predicted by a Kroupa IMF with Maraston (2005) SSPs for a solar metallicity burst and the effect that non-100% effective star-formation efficiencies (eSFEs) have on the model light-to-mass ratio (Goodwin & Bastian 2006).

standard IMF causes the photometric mass to differ from the dynamical mass. Since the discrepant clusters lie below the model line, they would have an over-abundance of low-mass stars with respect to the Kroupa IMF. Such bottom-heavy clusters are more likely to remain bound than clusters with a standard Kroupa IMF and should be apparent in the sample of old clusters. As they are not, this explanation seems unlikely for the majority of these young clusters. However, a non-standard IMF can not be ruled out in the case of NGC 1140–1.

There are various potential explanations for the difference between light-to-dynamical mass ratio and model light-to-mass ratio in the case of NGC 1140–1. These are explored below:

(i) Assuming that the difference between dynamical and photometric mass is due solely to the cluster being out of virial equilibrium, it can be seen from Fig. 7 that cluster 1 has an eSFE of around 10–20%. Goodwin & Bastian (2006) predict that a cluster with an eSFE of 10% will lose 80% of its mass in ~ 20 Myr and not remain bound. As such, the cluster would disperse over a relatively short timeframe and, therefore, not evolve into a second generation globular cluster.

(ii) An underestimate of the cluster extinction would have caused an underestimation of the photometric mass. How-

ever, in order to increase the luminosity of the cluster by the factor of ~ 9 required to match the photometric mass with the dynamical mass, the extinction would need to have been underestimated by around $E(B - V)_{\text{int}} \approx 0.9$ mag. Since the extinction calculated is in good agreement with previous measurements, and is already larger than the nebular extinction derived, this is unlikely to be the case.

(iii) Determining the half-light radii of the clusters was heavily dependent on the light profile adopted and several of the profiles were in good agreement with observation. However, adopting $r_{\text{hl}} \approx 6.0$ pc, the lowest potential half-light radius computed by ISHAPE for cluster 1, would still produce a virial mass that was a factor of seven larger than the photometric mass.

(iv) The crowded nature of the region may have caused the cluster velocity dispersion to be overestimated. The broadening of the RSG features seen in the knot spectra may not have been due solely to the virial motions of the brightest cluster within the knot, as is assumed, but may have had contributions from the motions of other clusters. This situation can be modelled using the template spectra, and a reduced χ^2 minimisation can be computed for this model knot. A template spectrum is broadened by 8 km s^{-1} to represent the broadening of cluster 1, as implied by its photometric mass and half-light radius. Added to this is the cluster 2 contribution, in the flux ratio of 1/1.7, as implied by the F814W photometry in Table 1. Taking the velocity dispersion of cluster 2 to be equal to that of cluster 1, the velocity dispersion found for knot A in Table 6 can be reproduced by introducing a relative velocity shift between the two clusters of $\sim 20 \text{ km s}^{-1}$. It is not possible to assess how likely such a shift is. Cluster 2 appears to be older than cluster 1 because of the lack of nebular emission (Fig. 1). This then implies that cluster 2 could have a larger photometric mass than cluster 1, despite its fainter luminosity, and thus have a larger velocity dispersion than adopted here. This would reduce the velocity shift required to produce a combined velocity dispersion equivalent to that observed for knot A. However, neither the photometric mass nor the shift are known and the importance of the contribution of cluster 2 to the velocity dispersion of knot A cannot be assessed.

It is not possible to quantify the degree to which these four factors contribute to the difference between the light-to-dynamical mass ratio measured and the model in Fig. 7. However, the contribution from the neighbours of cluster 1 is likely to be the most dominant factor for the large dynamical mass measured. As it is not possible to quantify this, it is also not possible to assess how long the cluster is likely to survive.

8.2 Young clusters as testing grounds of stellar evolution models

The nebular properties of the two knots of NGC 1140, and the massive star content of clusters 1 and 6 are presented in Table 8. There have been several other studies of young massive stellar populations of nearby starbursts, including the ultraviolet (UV) survey of Chandar, Leitherer & Tremonti (2004) and optical studies of Vacca & Conti (1992) and Schaerer, Contini & Kunth (1999a). However, the results of these surveys are not readily comparable to our results,

Table 8. Nebular knot properties and massive star content of NGC 1140 (this work), NGC 3125 (Hadfield & Crowther 2006) and Tol 89 (Sidoli et al. 2006).

Galaxy	NGC 1140		NGC 3125			Tol 89 (NGC 5398)	
Knot	A	B	A	B		A	B
$E(B - V)$ (mag)	0.16 ± 0.06	0.23 ± 0.08	0.16	0.13		0.07	0.29
N_e (cm $^{-3}$)	60 ± 50	—	140	140		90 ± 40	150 ± 40
T_e (K)	9700 ± 300	—	10500	9800		10000 ± 300	9800 ± 300
$12 + \log O/H$	8.29 ± 0.09	—	8.32	8.35		$8.27^{+0.08}_{-0.09}$	$8.38^{+0.06}_{-0.07}$
$N(O)^*$	6600 ± 2400	800 ± 500	4000	3200		685	2780
Age (Myr)	5 ± 1	> 10	~ 4	~ 4		3.5–4	< 2.5
Cluster	1	6	A1	A2	B1 + B2	A1	B1
$M_{\text{phot}} (10^6 M_\odot)$	1.1 ± 0.3	—	0.20	0.22	0.16	$0.1 - 0.2$	~ 0.03
$N(O)^\dagger$	5900 ± 1400	—	550	600	450	$310 - 680$	~ 100
$N(WN)$	550 ± 100	—	105	~ 55	40	80	—
$N(WC)$	200 ± 50	—	20	—	20	0	—
$N(WR)/N(O)$	0.1	—	0.2	0.1	0.1	0.2	—

* From the luminosity of the nebular $H\beta$ emission of the knot.

† From Starburst99, for the age and photometric mass of the cluster.

due to the different techniques adopted, especially in determining the WR populations.

Chandar et al. (2004) derived the O and WR content of the central starburst regions for a large sample of galaxies based upon UV *HST* spectroscopy and Starburst99 models. Fits to far-UV spectral morphologies and continuum slopes provided representative ages and extinctions from which O star populations were obtained, although individual clusters were not distinguished. The number of WR stars was inferred from a calibration of He II 1640 line luminosities. Individual clusters were also not considered in the ground-based optical studies of Vacca & Conti (1992) and Schaerer et al. (1999a). Standard nebular techniques were applied to derive extinctions, representative ages and O star numbers. WR populations resulted from calibrations of Galactic and LMC WR stars (Vacca 1994; Schaerer & Vacca 1998), which differ from our calibration with solely LMC templates.

Studies of individual massive clusters using common techniques, including *HST* imaging, have been carried out by Hadfield & Crowther (2006) and Sidoli et al. (2006) for two galaxies of LMC-like metallicity, the blue compact dwarf galaxy NGC 3125 and the giant HII region (GHR) Tol 89 located in the barred spiral galaxy NGC 5398. A comparison of individual knots, as derived from nebular properties, and cluster masses and O star numbers, from Starburst99 modelling, is made in Table 8. WR populations follow from optical calibrations of Crowther & Hadfield (2006) in all cases.

NGC 1140–1 is a significantly more massive counterpart to NGC 3125–A1 and Tol 89–A1, with a similar, high ratio of WR to O type stars, $N(WR)/N(O) \sim 0.1 - 0.2$ and $N(WC)/N(WN) \leq 0.4$. These empirical stellar populations can be compared to predictions from evolutionary synthesis models (e.g. Starburst99), for which reduced WR populations of $N(WR)/N(O) \sim 0.02 - 0.1$ and a substantially different subtype distribution of $N(WC)/N(WN) \sim 40$ are predicted. These are based on standard Geneva evolution models (Meynet et al. 1994) for ages of 4 – 5 Myr (see also Sidoli et al. 2006). Allowance for rotational mix-

ing in evolutionary models does not resolve these discrepancies, i.e. $N(WR)/N(O) < 0.1$ and $N(WC)/N(WN) \sim 10$ according to Vázquez et al. (2007) for a 5 Myr old population at $Z = 0.008$. Padova models (Fagotto et al. 1994) also predict a low ratio of WR to O stars, with $N(WR)/N(O) \sim 0.04 - 0.07$. These models, however, predict significantly more realistic ratios of WC to WN stars of $N(WC)/N(WN) \sim 0.2 - 2$ between 4 – 5 Myr.

9 SUMMARY

We present new high spectral resolution VLT/UVES spectroscopy and *HST*/ACS imaging of the central region of NGC 1140. It is apparent from the ACS imaging that the central region contains several clusters, although this is only resolved into two star-forming knots by the UVES spectroscopy: knot A, which contains clusters 1 and 2, and knot B, which contains clusters 5, 6 and 7.

Nebular analysis of knot A yields an LMC-like metallicity of $12 + \log O/H = 8.29 \pm 0.09$. Starburst99 modelling indicates an age of 5 ± 1 Myr and a photometric mass of $(1.1 \pm 0.3) \times 10^6 M_\odot$ for cluster 1. Virial masses of $(10 \pm 3) \times 10^6 M_\odot$ and $(9.1 \pm 0.8) \times 10^6 M_\odot$ were determined for clusters 1 and 6, respectively, using the half-light radii determined from the F625W ACS image and the velocity dispersions determined by computing a reduced- χ^2 minimisation between the cluster spectrum and RSG template spectra over a spectral region containing the Ca II triplet. We interpret the difference between the dynamical and photometric mass of cluster 1 as due to the crowded nature of knot A: the velocity dispersion measured may not relate only to cluster 1, as assumed, but likely contains a component that arises from cluster 2, with a different systemic velocity to cluster 1.

We find 6600 and 800 O stars within knots A and B, respectively, from the $H\beta$ luminosities of the knots. Our Starburst99 model predicts 5900 O stars within cluster 1. This implies that $> 90\%$ of the O stars within knot A are contained in cluster 1. Empirical fitting of the

blue bump of cluster 1 indicates that this cluster contains around 550 WN stars and 200 WC stars, giving ratios of $N(\text{WR})/N(\text{O}) = 0.1$, if all of the WR stars lie within cluster 1, and $N(\text{WC})/N(\text{WN}) = 0.4$. The observed ratio of WR stars to O stars is significantly larger than predicted by current evolutionary models. The observed ratio of WC to WN stars is reproduced more successfully using Padova instantaneous burst models than Geneva models, even allowing for rotational mixing.

ACKNOWLEDGMENTS

SM acknowledges financial support from PPARC/STFC. The Image Reduction and Analysis Facility IRAF is distributed by the National Optical Astronomy Observatories, which is operated by the Association of Universities for Research in Astronomy, Inc., under cooperative agreement with the U.S. National Science Foundation. We would like to thank Søren Larsen for his help with the ISHAPE analysis and Fabrizio Sidoli, who provided help with the UVES data reduction. We would also like to thank Nate Bastian and Simon Goodwin for supplying their effective star formation efficiency models and for discussions on the subject.

REFERENCES

- Bastian N., Saglia R. P., Goudfrooij P., Kissler-Patig M., Schweizer F., Zoccali M., 2006, *A&A*, 448, 881
- Boily C. M., Lançon A., Deiters S., Heggie D. C., 2005, *ApJ*, 620, L27
- Chandar R., Leitherer C., Tremonti C. A., 2004, *ApJ*, 604, 153
- Crowther P. A., 2007, *ARA&A*, 45, 177
- Crowther P. A., Hadfield L. J., 2006, *A&A*, 449, 711
- de Grijs R., Parmentier G., 2007, *ChJA&A*, 7, 155
- de Grijs R., Smith L. J., Bunker A., Sharp R. G., Gallagher III J. S., Anders P., Lançon A., O’Connell R. W., Parry I. R., 2004, *MNRAS*, 352, 263
- de Vaucouleurs G., de Vaucouleurs A., Corwin H. G. J., Buta R. J., Paturel G., Fouqué P., 1991, *Third Reference Catalogue of Bright Galaxies*, Version 3.9
- Díaz A. I., Terlevich E., Terlevich R., 1989, *MNRAS*, 239, 325
- Elson R. A. W., Fall S. M., Freeman K. C., 1987, *ApJ*, 323, 54
- Fagotto F., Bressan A., Bertelli G., Chiosi C., 1994, *A&AS*, 105, 29
- Fleck J.-J., Boily C. M., Lançon A., Deiters S., 2006, *MNRAS*, 369, 1392
- Goodwin S. P., Bastian N., 2006, *MNRAS*, 373, 752
- Gray D. F., Toner C. G., 1986, *ApJ*, 310, 277
- Guseva N. G., Isotov Y. I., Thuan T. X., 2000, *ApJ*, 531, 776
- Hadfield L. J., Crowther P. A., 2006, *MNRAS*, 268, 1822
- Haynes M. P., Hogg D. E., Maddalena R. J., Roberts M. S., van Zee L., 1998, *AJ*, 115, 62
- Heckman T. M., 1998, in Woodward C., Shull J., Thronson H., eds, *Starbursts: Lessons for the Origin and Evolution of Galaxies and the Intergalactic Medium ASP Conference Series vol. 158*, San Francisco, p. 127
- Ho L. C., Filippenko A. V., 1996a, *ApJ*, 466, L83
- Ho L. C., Filippenko A. V., 1996b, *ApJ*, 472, 600
- Howarth I. D., 1983, *MNRAS*, 203, 301
- Hummer D. G., Storey P. J., 1987, *MNRAS*, 224, 801
- Hunter D. A., O’Connell R. W., Gallagher III J. S., 1994a, *AJ*, 108, 84
- Hunter D. A., van Woerden H., Gallagher III J. S., 1994b, *ApJS*, 91, 79
- Izotov Y. I., Thuan T. X., 2004, *ApJ*, 602, 200
- Kennicutt R. C., 1998, *ARA&A*, 36, 189
- King I. R., 1962, *AJ*, 67, 471
- Krist J., Hook R., 1997, *The Tiny Tim User’s Guide*. STScI, Baltimore
- Kroupa P., 2002, *Science*, 295, 82
- Larsen S. S., 1999, *A&AS*, 139, 393
- Larsen S. S., Richtler T., 2004, *A&A*, 427, 495
- Leitherer C., Schaerer C., Goldader J. D., González Delgado R. M., Robert C., Kune D. F., de Mello D. F., Devost D., Heckman T. M., 1999, *ApJS*, 123, 3
- Maraston C., 2005, *MNRAS*, 362, 799
- Maraston C., Bastian N., Saglia R. P., Kissler-Patig M., Schweizer F., Goudfrooij P., 2004, *A&A*, 416, 176
- Massey P., Olsen K. A. G., 2003, *AJ*, 126, 2867
- Mengel S., Lehnert M. D., Thatte N., Genzel R., 2002, *A&A*, 383, 137
- Meynet G., Maeder A., Schaller G., Schaerer D., Charbonnel C., 1994, *A&AS*, 103, 97
- Nagao T., Maiolino R., Marconi A., 2006, *A&A*, 459, 85
- O’Connell R. W., Gallagher III J. S., Hunter D. A., 1994, *ApJ*, 433, 65
- Östlin G., Cumming R. J., Bergvall N., 2006, *A&A*, 261, 471
- Russell S. C., Dopita M. A., 1990, *ApJS*, 74, 93
- Schaerer D., Contini T., Kunth D., 1999a, *A&A*, 341, 399
- Schaerer D., Contini T., Pindao M., 1999b, *A&AS*, 136, 35
- Schaerer D., Vacca W. D., 1998, *ApJ*, 497, 618
- Schlegel D. J., Finkbeiner D. P., Davis M., 1998, *ApJ*, 500, 425
- Sidoli F. X., Smith L. J., Crowther P. A., 2006, *MNRAS*, 370, 799
- Sirianni M. et al. 2005, *PASP*, 117, 836
- Spitzer L., 1987, *Dynamical Evolution of Globular Clusters*. Princeton University Press, Princeton
- Tonry J., Davis M., 1979, *AJ*, 84, 1511
- Vacca W., 1994, *ApJ*, 421, 140
- Vacca W. D., Conti P. S., 1992, *ApJ*, 401, 543
- Vázquez G. A., Leitherer C., 2005, *ApJ*, 621, 695
- Vázquez G. A., Leitherer C., Schaerer D., Meynet G., Maeder A., 2007, *ApJ*, 663, 995
- Walcher C. J., van der Marel R. P., McLaughlin D., Rix H. W., Böker T., Häring N., Ho L. C., Sarzi M., Shields J. C., 2005, *ApJ*, 618, 237
- Westmoquette M. S., Smith L. J., Gallagher III J. S., Exter K. M., 2007, *MNRAS*, accepted